Comparative Study of Nickel-Iron Composite with Fe_3O_4 Nanoparticles for the Adsorption of Chromium from Aqueous Medium

Anjali Yadav · Sapna Raghav ·
Anamika Srivastava · Nirmala Kumari Jangid ·
Manish Srivastava

Abstract Water contamination caused by hexavalent chromium [Cr(VI)] ions has attracted interest since Cr(VI) ions are highly poisonous and carcinogenic, posing major health risks. We report a simple and efficient approach for preparing Fe_3O_4 nanoparticles and Fe_3O_4/NiO composite using the chemical co-precipitation method for Cr(VI) removal. The produced magnetic adsorbents could be readily isolated from the solution using an external magnet and were used for Cr(VI) ion adsorption. The adsorbents were characterized by XRD, VSM, FT-IR, FE-SEM, EDX, and BET analyses. The Langmuir type 1 isotherm provided a good representation of the adsorption data when the Langmuir, Freundlich, Temkin, Harkins–Jura, Hasley, and Redlich-Peterson models were utilized to analyze the adsorption isotherm data. The adsorption capacities of Fe_3O_4 and Fe_3O_4/NiO composite calculated from the Langmuir type 1 model were 96.15 mg g^{-1} and 150 mg g^{-1}, respectively. The saturation magnetization of Fe_3O_4 and Fe_3O_4/NiO composite was 60.54 emu/g and 11.09 emu/g, respectively. Both adsorbents may be easily and quickly separated from tainted water by an external magnetic field. According to the findings, both adsorbents are possibly reusable adsorbents for Cr(VI) adsorption. The main advantage of the material is that, due to its magnetic nature, it is easily separated from the adsorbate and may thus be used efficiently in sorption studies. As a result, this magnetic adsorbent provides a viable solution for the successful management of chromium-containing wastewater.

Keywords Fe_3O_4 nanoparticles · Cr(VI) adsorption. Desorption of Cr(VI) · Wastewater

A. Yadav · A. Srivastava · N. K. Jangid
Department of Chemistry, Banasthali Vidyapith,
Banasthali 304022, Rajasthan, India

S. Raghav
Department of Chemistry, Mewar University, Chittorgarh,
Rajasthan 312901, India

M. Srivastava (✉)
Department of Chemistry, University of Allahabad,
Prayagraj 211002, India
e-mail: sagermanish1@gmail.com

1 Introduction

Indeed, the current prosperity of industries has evident positive effects on economic growth, but the release of industrial wastes into water bodies without proper treatment has the potential to wipe out humanity (Eltaweil et al., 2021). The typical contaminants, like heavy metal ions and organic dyes, often co-exist in polluted water and have significant ecological effects on the ecosphere because of their bio-accumulation, non-biodegradability, and environmental persistence (Tang et al., 2021; Wen et al., 2019).

A severe concern for the environment and human health is heavy metal contamination. Metals are generally non-biodegradable and enter the environment

through a variety of anthropogenic and natural sources. Chromium has recently gained a lot of interest among heavy metals due to its toxicity in the environment (Imran et al., 2020). Long-term exposure to high chromium concentrations increases the risk of diabetes, skin disease, respiratory illness, and gastro-intestinal disease. The most common oxidation states of chromium in nature are Cr(III) and Cr(VI) (Manoj et al., 2021; Rahman & Singh, 2019; Teklay, 2016). Many scientists are interested in Cr(VI) since it is a common carcinogen that results in negatively charged compounds with great environmental mobility (Yao et al., 2020; Zou et al., 2021). As a result, removing Cr(VI) from aqueous solutions before releasing them into the environment becomes essential (Pourmortazavi et al., 2019; Shekhawat et al., 2022).

Various techniques, including ion exchange, ultra-filtration, coagulation, electrodeposition, reverse osmosis, chemical precipitation, and solvent extraction, have been developed by researchers to eliminate hexavalent chromium ions from wastewater. However, these methods have significant disadvantages and are not completely suitable for Cr(VI) adsorption. Owing to its flexibility, low cost, high efficiency, and simple operation, adsorption technology is recognized as the best technique among these (Pavithra et al., 2021).

A solid material that permits liquid or gaseous molecules to adhere to its surface is known as an adsorbent. The adsorbent surface's chemical and physical characteristics, in addition to the soluble compounds' qualities, determine the adsorbent's performance. A good adsorbent material should have both a minimal volume and a wide surface area. High mechanical strength, chemical and thermal stability, high porosity, and small pore diameter—which result in more exposed surface area and, consequently, appropriate surface chemistry that leads to high adsorption capacity—must be among the other characteristics. To suit the needs of the application, adsorptive materials can be designed as pellets, rods, moldings, or monoliths. Adsorbents made of a variety of materials have been employed for a wide range of purposes, including desiccants, water treatment, separation, catalysis, and indicators (Abegunde et al., 2020; Younas et al., 2021).

Metal-contaminated wastewater is frequently treated using a variety of porous adsorbents, including activated carbon, natural clay, chitosan composite, nanoparticle and polymer-based adsorbents, magnetic adsorbents, etc. (Abbas & Hussain, 2016; Abbas et al., 2015; Arora et al., 2019; Kobielska et al., 2018; Lodhi et al., 2019; Soni et al., 2020a; Wang et al., 2023; Yan et al., 2020).

Several studies have been carried out to investigate the usage of magnetic adsorbents as a safe, effective, and low-cost material for separating these suspended adsorbents in wastewater. The variation in the response of magnetic substances to outside magnetic fields is associated with a variety of characteristics, since certain substances are much more magnetic than others. Magnetic nanoparticles (MNPs) have recently been identified as outstanding adsorbents for the elimination of heavy metals. However, magnetism is not the only consideration for their application. When compared to other materials, their exceptional surface charge and redox activity properties are significant reasons for their qualification.

Fe_3O_4 nanoparticles have gained interest as a type of magnetic nanoparticle due to their unique magnetic characteristics and ease of preparation. But Fe_3O_4 nanoparticles are prone to agglomerate and lose their magnetic characteristics, which decreases the efficiency of removal. Significant attempts have been made to modify Fe_3O_4 nanoparticles using physicochemical approaches in order to overcome these drawbacks, retain their magnetic properties, and improve their adsorption performance and specific stability (Abdullah et al., 2019; Mohammadi et al., 2021; Sharma et al., 2019; Song et al., 2021; Zhao et al., 2021).

In this study, we present the use of Fe_3O_4 nanoparticles and Fe_3O_4/NiO composite as efficient materials for the elimination of Cr(VI). Parameters affecting the adsorption process, viz., the adsorbent's dose, contact time, pH, initial concentration, temperature effect, and regeneration study, were evaluated to understand the mechanism. The material was examined using BET, XRD, FT-IR, FE-SEM, EDX, and vibrating-sample magnetometer (VSM) analysis in order to determine its chemical composition and surface characteristics. The use of Fe_3O_4 nanoparticles and Fe_3O_4/NiO composite as potential adsorbents for Cr(VI) removal was further probed using kinetic and isotherm models. Moreover, the reusability of both adsorbents was examined for up to six cycles.

2 Experimental Section and Adsorption Experiment

2.1 Materials

All analytical grade chemicals as well as reagents were purchased from Sigma-Aldrich and utilized immediately without any additional refining. During the synthesis and adsorption studies, iron (II) chloride tetrahydrate, nickel (II) nitrate hexahydrate, iron (III) chloride hexahydrate, sodium hydroxide, and acetone were utilized. $K_2Cr_2O_7$ was purchased from E. Merck, India. All aqueous solutions for the adsorption studies were prepared using Millipore Milli-Q® ultrapure water. As Cr(VI) has been chosen as the model contaminant in this investigation, solution of Cr(VI) if desired concentrations were prepared and used as adsorbate solution.

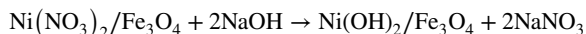### 2.2 Preparationof Fe_3O_4 Nanoparticles

4.75 g of iron (II) chloride tetrahydrate and 9 g of iron (III) chloride hexahydrate salts were added in 100 mL of deionized (DI) water. In this synthesis process, the stoichiometry of $FeCl_2 \cdot 4H_2O/FeCl_3 \cdot 6H_2O$ was 1:2. The reaction was conducted in a N_2 environment at 80 °C while being vigorously stirred. A 25-mL aliquot of sodium hydroxide solution was dropped into the mixture while it was still being stirred, resulting in a pH of 10 and the production of a black precipitate. The resulting solution was then centrifuged three times with deionized (DI) water and then with acetone. External magnet was used to collect the

Fe_3O_4 nanoparticles and then it was rinsed with water (Fig. 1) (Mohammadi et al., 2021; Weber & Morris, 1963).

$$Fe^{2+}(aq) + 2Fe^{3+}(aq) + 8OH^-(aq) \rightarrow Fe_3O_4(s) + 4H_2O$$

2.3 Preparation of Fe_3O_4/NiO Composite

Fe_3O_4/NiO composite was prepared by the co-precipitation technique. 3.1 g of $Ni(NO_3)_2 \cdot 6H_2O$ and 0.31 g of Fe_3O_4 nanoparticles were added to 20.0 mL of water. The solution's temperature was then raised to 75 °C using a magnetic stirrer. The second step was adding 20 mL of NaOH to original solution dropwise until a black-green suspension was attained and stirred for 60 min. After 60 min, a powerful magnet was used to remove the composite from the solution. They were then thoroughly washed with acetone and DI water and placed in an oven at 60 °C show in Fig. 2 (Hassan & Hrdina, 2022).

$$Ni(NO_3)_2/Fe_3O_4 + 2NaOH \rightarrow Ni(OH)_2/Fe_3O_4 + 2NaNO_3$$

2.4 Adsorption Experiments

Using the required chromium stock solution, adsorption studies were conducted to assess the tendency of Fe_3O_4 nanoparticles and Fe_3O_4/NiO composite for adsorption. In addition, several optimal conditions involving significant factors such as pH (4–9), adsorbent dose (0.01–0.14 g/L), contact time (5–70 min), and initial chromium concentration (2–20 mg/L) were
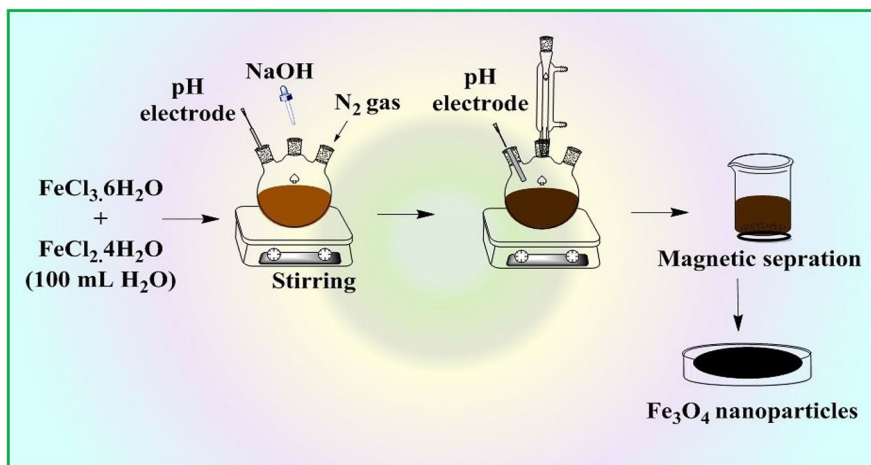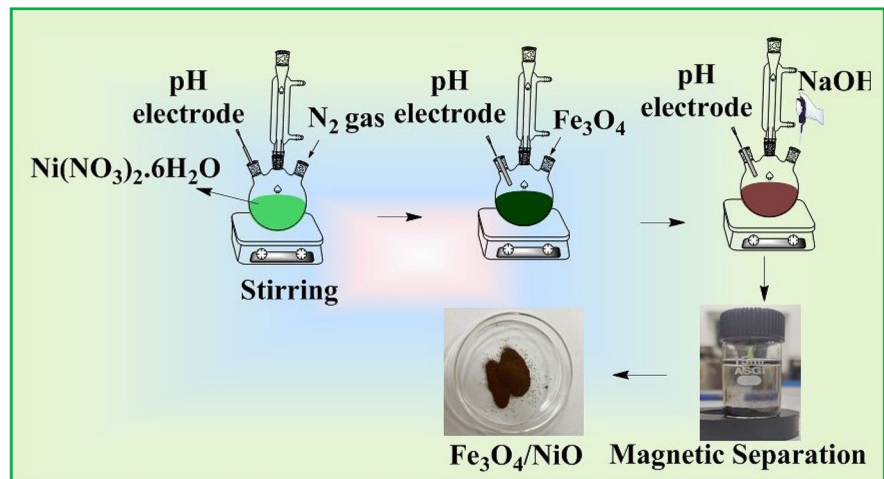
Fig. 1 Preparation of Fe_3O_4 nanoparticles

Fig. 2 Preparation of Fe₃O₄/NiO composite

studied. NaOH and HCl solutions were used to equilibrate the pH. Proceeding adsorption, the remaining chromium concentration was analyzed by AAS. Using Eqs. (1) and (2), the adsorption percent and equilibrium absorption of Cr(VI) by Fe₃O₄ nanoparticles and Fe₃O₄/NiO composite from aqueous solution were calculated.

$$\% \, Adsorption = \frac{(C_0 - C_e) \times 100}{C_0} \qquad (1)$$

$$Adsorption \, Capacity \left(q_e \right) = \frac{(C_0 - C_e) \times V}{m} \qquad (2)$$

where q_e is the adsorption capacity at equilibrium (mg/g), C_0 represents the initial Cr(VI) concentration (mg/L), C_e is the equilibrium Cr(VI) concentration, V is the volume of the solution (L), and m is the mass of the adsorbent (g) (Li et al., 2021).

2.5 Characterization

XRD of the Fe₃O₄ nanoparticles and Fe₃O₄/NiO composite were recorded on Bruker D8 Discover X-ray diffractometer using Cu Kα radiation. For XRD analysis, powdered and degassed samples were directly put on the sample disk of XRD and then exposed to the X-ray source. The XRD pattern was recorded in the 2θ range of 10° and 70°. XRD studies revealed the crystalline character of the adsorbents. By using surface area analyzer (Quantachrome Autosorb iQ surface analyzer), N₂ adsorption–desorption studies were carried out to characterize their textural properties (pore volume and the BET specific surface area). For the analysis of surface area, the samples were first degassed for 3.0 h to remove volatile gases and were then placed in surface area analyzer for N₂ adsorption–desorption. The FTIR spectra were recorded using a Perkin-Elmer FT-IR spectrometer. A spectrum of the adsorbents in the 400–4000 cm⁻¹ range to characterize the type of surface functional groups and the nature of chemical bonding. For the functional group analysis, the samples were first mixed with KBr powder and the sample pellets with KBr were prepared in the form for thin films using a pelletizer. Then the sample was placed in the FTIR chamber for analysis. A field emission scanning electron microscope was used to investigate the morphology of Fe₃O₄ nanoparticle and Fe₃O₄/NiO composite as well as their elemental composition. FE-SEM equipped with EDX (FE-SEM, MIRA3 TESCAN, and an INCA Energy X-MAX-50) was used to characterize the morphology and chemical composition of the adsorbents used in the study. For FE-SEM analysis, the adsorbents were first coated on carbon tape present on the sample holder, so as to make them conductive, and then the stub with the sample was placed in the FE-SEM chamber for study. The magnetic characteristics of the adsorbents were determined using a LakeShore 7404 VSM. The magnetic sample is mounted on the sample holder and placed between the electromagnetic poles, generally horizontally, for VSM measurement. At the ambient temperature, the hysteresis loops were measured on the VSM.

3 Results and Discussion

3.1 BET Surface Area

The N_2 gas adsorption–desorption isotherm was observed in the relative pressures (p/p_0) values to estimate the surface area and porosity values of the synthesized adsorbents. BET sorptometry was performed to study the pore volume, average pore size, and surface area of the material. The N_2 adsorption–desorption curves for the Fe_3O_4 nanoparticles and Fe_3O_4/NiO composite are depicted in Fig. 3, and their characteristic parameters are listed in Table 1. Furthermore, this figure shows that Fe_3O_4 nanoparticles and Fe_3O_4/NiO composites follow the IUPAC type (IV) isotherm. In other words, it denotes a structure with the mesoporous nature of the adsorbents (Koohi et al., 2021; Mohammadi et al., 2021). The surface area of synthesized Fe_3O_4 nanoparticles and Fe_3O_4/NiO composites is equivalent to 110.7 m^2 g^{-1} and 163.9 m^2 g^{-1}, respectively. The Langmuir surface area and total pore volume of Fe_3O_4 nanoparticles and Fe_3O_4/NiO composites were 171.9 m^2 g^{-1}, 287.4 m^2 g^{-1}, and 0.484 cm^3 g^{-1}, 0.327 cm^3 g^{-1}, respectively. The average pore size of the Fe_3O_4 nanoparticles and Fe_3O_4/NiO composite was 87.42 Å and 39.92 Å, respectively.

Table 1 Surface parameters of Fe_3O_4 nanoparticle and Fe_3O_4/NiO composite before Cr(VI) adsorption

Parameters	Fe_3O_4	Fe_3O_4/NiO
Specific surface area (m^2/g)	110.7	163.9
Langmuir surface area (m^2/g)	171.9	287.4
Average pore size (Å)	87.42	39.92
Total pore volume (cc/g)	0.484	0.327

As a result, the higher the surface area, the greater will be the adsorption capacity.

3.2 Fourier Transform Infrared Spectroscopy

For understanding the nature of chemical bonding and the kinds of surface functionalities, the adsorbents used in this study were examined by FT-IR. The FT-IR spectra of Fe_3O_4 nanoparticles and Cr(VI)-loaded Fe_3O_4 nanoparticles are demonstrated in Fig. 4a. Likewise, the FT-IR spectra of the Fe_3O_4/NiO composite before and after the adsorption process are demonstrated in Fig. 4b.

The distinctive peaks of nanoparticles are visible in the FT-IR spectra of Fe_3O_4 nanoparticles. The tensile vibrations of the Fe–O and Ni–O bonds were measured between 500 and 650 cm^{-1}. This band is
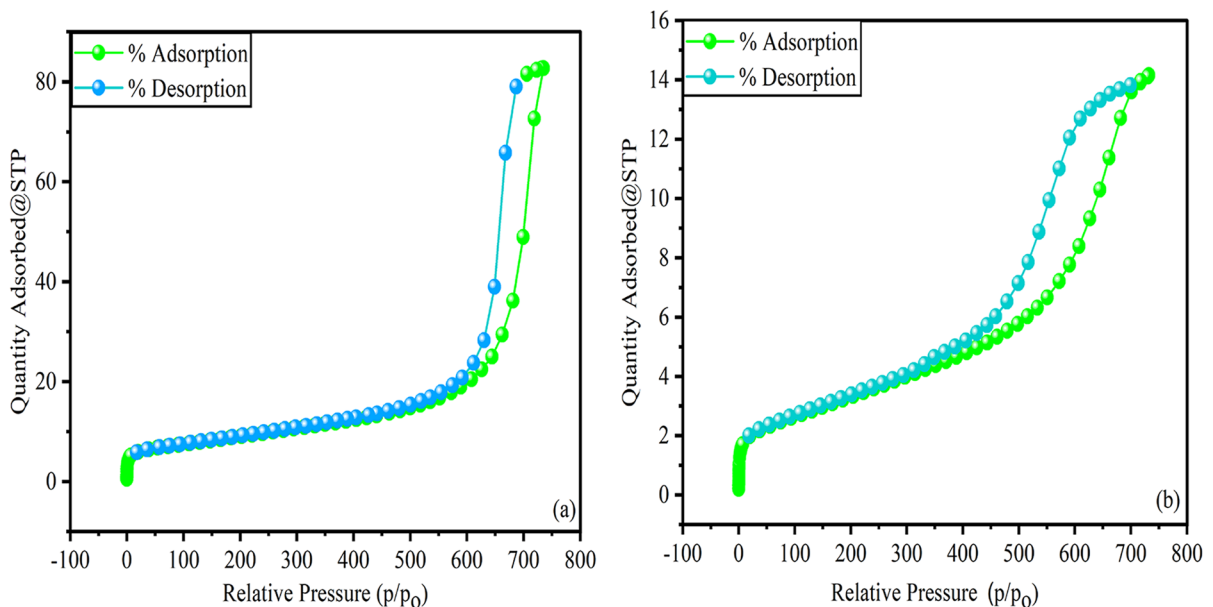

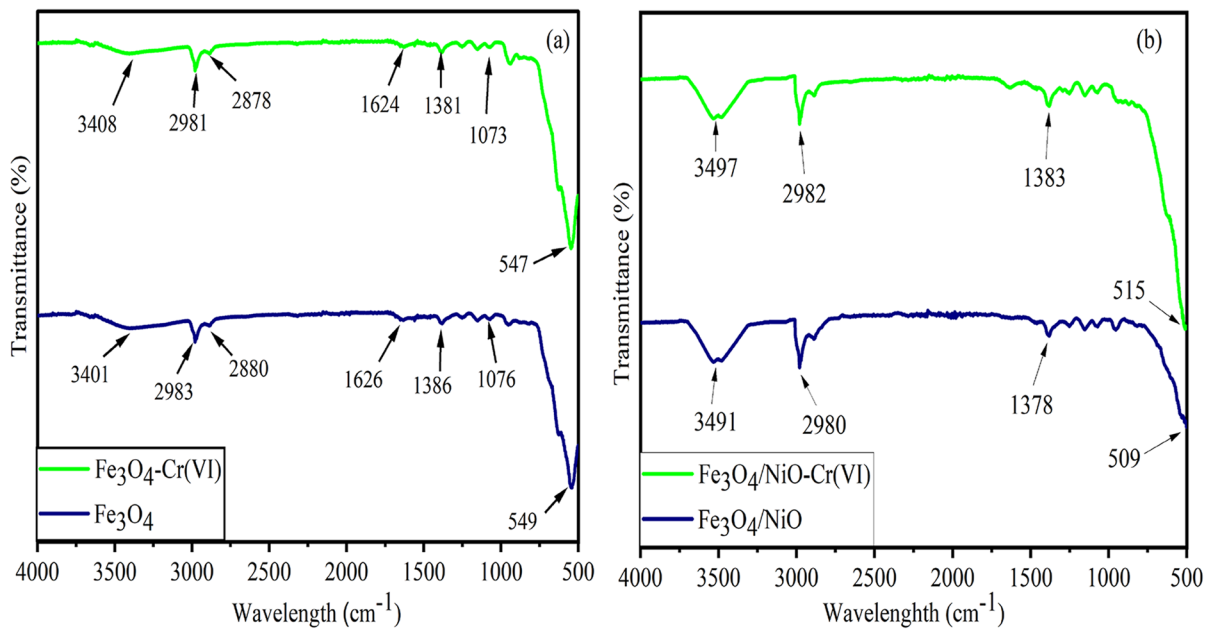**Fig. 3** N_2 sorption isotherm of **a** Fe_3O_4 nanoparticle, **b** Fe_3O_4/NiO composite

Fig. 4 FTIR spectra of **a** Fe_3O_4 nanoparticles and **b** Fe_3O_4/NiO composite (before and after Cr(VI) adsorption)

very sharp and has strong intensity, indicating the crystallinity of the sample.

The broad bands around 3401 cm^{-1} and 1626 cm^{-1} were due to the O–H stretching vibration of surface-adsorbed water molecules. The bands located around 1386 cm^{-1} and 1076 cm^{-1} were attributed to the asymmetric and symmetric stretching vibrations of COO^- (Fig. 4a). The O–H stretching vibration of surface-adsorbed water molecules is responsible for the broad band around 3491 cm^{-1} (Fig. 4b) (Chaki et al., 2015; Mahdavi & Amini, 2016; Munkaila et al., 2021; Nodehi et al., 2022; Shi et al., 2020).

After Cr(VI) adsorption, there is a minor shift in the band centered at 549 cm^{-1}, corresponding to the

Fe–O bonds, which changes to 547 cm^{-1}, suggesting the formation of Fe–O–Cr on the magnetite surface. Peak values in Fe_3O_4 and Fe_3O_4/NiO composites showed significant changes in Table 2.

3.3 X-ray Diffraction

To understand more about the chemical and physical composition of the magnetic particles, X-ray diffraction (XRD) is a highly valuable technique. Figure 5 represents the XRD pattern of Fe_3O_4 nanoparticle and Fe_3O_4/NiO composite. The crystalline phase of Fe_3O_4 nanoparticle and Fe_3O_4/NiO composite was analyzed by XRD.

Table 2 FTIR spectra of Fe_3O_4 nanoparticle and Fe_3O_4/NiO composite

IR wavenumbers (cm^{-1})		Assignment of absorption bands
Fe_3O_4 nanoparticles	Fe_3O_4/NiO composite	
3401 cm^{-1} and 1626 cm^{-1}	3491 cm^{-1}	O–H stretching vibration of surface-adsorbed water molecules
1386 cm^{-1} and 1076 cm^{-1}	1378 cm^{-1}	Asymmetric and symmetric stretching vibrations of COO^-
549 cm^{-1}	509 cm^{-1}	M–O bonds
547 cm^{-1}	515 cm^{-1}	M–O–Cr bonds

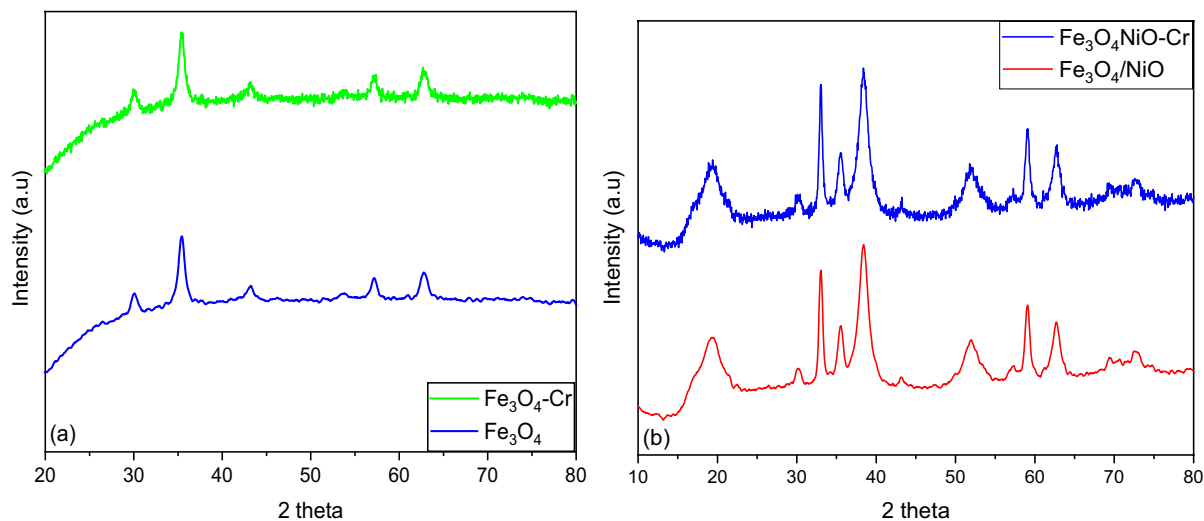**Fig. 5** XRD spectra for **a** Fe₃O₄ nanoparticle and **b** Fe₃O₄/NiO composite (before and after Cr(VI) adsorption)

It was notable that Fe_3O_4 nanoparticles showed XRD pattern with diffraction peaks at $2\theta = 30.1°$, $35.5°$, $43.2°$, $53.6°$, $57.3°$, and $62.7°$ relative to the diffractions of (220), (311), (400), (422), (511), and (440) crystal faces of Fe_3O_4 (Mohammadi et al., 2021). The peaks at $2\theta = 30.1°$, $33.03°$, $35.5°$, $38.38°$, $43.23°$, $51.8°$, $57.2°$, $59.09°$, $62.7°$, $75°$, and $79.4°$ are associated with Fe_3O_4/NiO composite. The crystal plane of NiO is (1 1 1), (2 0 0), (2 2 0), (2 2 2), and (4 0 0) (Ashan et al., 2018; Koohi et al., 2021; Mahdavi & Amini, 2016). The crystallite size of produced Fe_3O_4-NPs can be estimated using the Debye–Scherrer equation, which demonstrates a link between X-ray diffraction peak broadening and crystallite size. The Debye–Scherrer equation is presented as follows:

$$d = \frac{k\lambda}{\beta_{hkl}\cos\theta_{hkl}}$$

The equation for manufactured Fe3O4 NPs for (hkl) phase is as follows: *d* is the crystallite size, *k* is the Scherrer constant (0.9), λ is the X-ray wavelength of radiation for Cu Kα (0.154 nm), βhkl is the full-width at half maximum (FWHM) at (hkl) peak in radian, and θ hkl is the diffraction angle for the (hkl) phase. The crystallite size of synthesized Fe_3O_4 NPs was determined to be 6.25 nm using an equation based on the full-width at half maximum of the Fe_3O_4 (311) diffraction peak at $2\theta = 35.35°$. Based on the X-ray diffraction pattern, the produced Fe_3O_4 NPs

were determined to be high purity crystalline, with no impurity peak detected.

3.4 FE-SEM Analysis

The morphology of Fe_3O_4 nanoparticles and Fe_3O_4/NiO composite was investigated using FE-SEM, and the elemental composition was determined using EDX. SEM and EDX images of both are displayed in Fig. 6. The spherical-shaped particles with agglomeration were observed in synthesized Fe_3O_4 nanoparticles (Fig. 6a). In Fig. 6b, the synthesized composite particles are distributed relatively uniformly. Also, the particles are strongly clumped together. The inserted figure shows the porosity in the Fe_3O_4/NiO composite. Figure 6c and d depict the corresponding EDX spectra, which show the elemental composition of Fe_3O_4 nanoparticles and Fe_3O_4/NiO composites (Mohammadi et al., 2021; Nodehi et al., 2022).

3.5 Magnetization

To evaluate the adsorbents' magnetic properties, VSM tests was utilized (Ashan et al., 2018). Magnetization curves were utilized to examine the magnetic properties of the magnetic materials under investigation. Figure 7 illustrates the magnetization curves of Fe_3O_4 nanoparticles, Fe_3O_4/NiO, and Fe_3O_4/NiO-Cr(VI) composites. The saturation magnetization
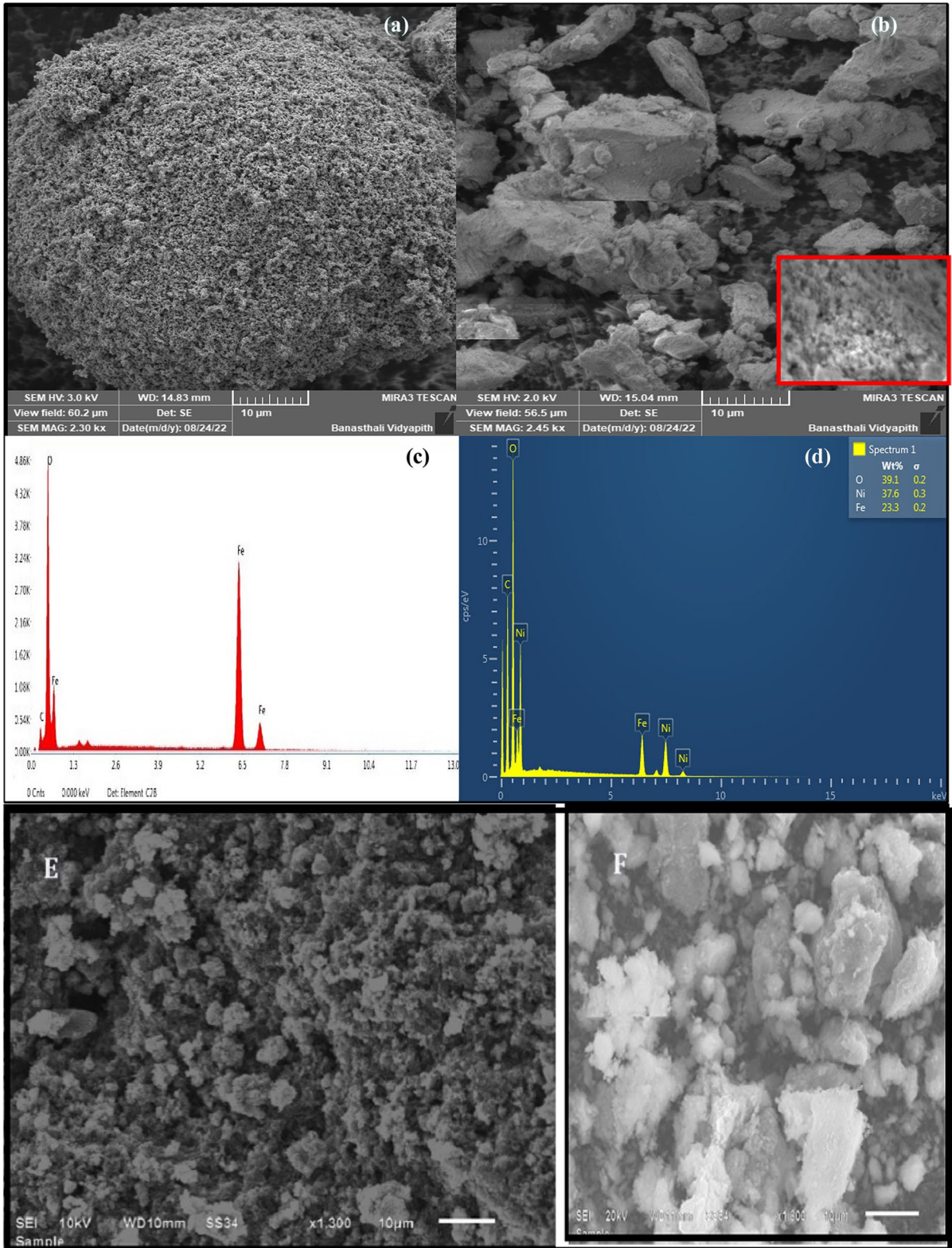
◄**Fig. 6** FESEM image of **a** Fe_3O_4 nanoparticles, **b** Fe_3O_4/NiO composite, and EDX image of **c** Fe_3O_4 nanoparticles, **d** Fe_3O_4/NiO composite, **e** Fe_3O_4 nanoparticles after absorption Cr, **f** Fe_3O_4/NiO composite after absorption Cr

of the Fe_3O_4 nanoparticle and Fe_3O_4/NiO composite was 60.54 emu/g and 11.09 emu/g, respectively, though, even at this saturation magnetization value, a magnetic field is sufficient to separate the adsorbent from the aqueous medium (Mahmoudi & Behnajady, 2018). The existence of a non-magnetic shell reduces the magnetization of the Fe_3O_4/NiO composite. The shell's interaction with Fe_3O_4 nanoparticle surface locks of the surface spins, lowering magnetic torque in the Fe_3O_4/NiO composite. Because lowering the size of the particle leads to an increase in the proportion of surface atoms, even minor irregularities in the surface layers have a significant impact on nanoparticle magnetic saturation (Nodehi et al., 2022).

3.6 Zeta Sizer

The particle size distribution of Fe_3O_4 nanoparticles was analyzed using zeta sizer. The particle size distribution nanoparticles was found to be 180.7 nm.

Zeta potential further confirmed the successful fabrication of Fe_3O_4 nanoparticles. The zeta potential of Fe_3O_4 nanoparticles was -22.7 eV show in Fig. 8.

3.7 Study of Kinetics of Adsorption of Cr(VI) on to the Adsorbents, Fe_3O_4 Nanoparticle, and Fe_3O_4/NiO Composite

Adsorption kinetics explains how the material's chemical and physical characteristics affect the reaction's rate and pathways. Using the pseudo-first-order (PFO) and pseudo-second-order (PSO) models, the kinetics of adsorption were explained.

Adsorption in a solid–liquid system was described using the PFO kinetic model. According to this model, one metal ion is adsorbed per sorption site on the adsorbent's surface (Suo et al., 2019). PFO is represented by

$$\ln\left(q_e - q_t\right) = \ln q_e - k_1 \times t \tag{3}$$

where k_1 (min^{-1}) is the PFO sorption rate constant.

The kinetic plot for PFO for Cr(VI) adsorption was obtained by plotting $\ln(q_e - q_t)$ against t. The rate constant and equilibrium adsorption capacity were calculated using the slope and intercept (Fig. 9a).

In accordance with the PSO model, one metal ion is adsorbed onto two sorption sites on the adsorbent's surface. This model has been utilized to investigate the kinetics of chemisorption from liquid solutions (Almomani & Bhosale, 2021; Bin-Dahman & Saleh, 2024). PSO is represented as

$$t/q_t = 1/(k_2 \times q_e^2) + t/q_e \tag{4}$$

where k_2 ($g\ mg^{-1}\ min^{-1}$) is the PSO rate constant. The graph displayed between t/q_t and t in Fig. 9b produces a straight line, and the slope and intercept may be used to get the values of q_e and k_2, respectively (Khare et al., 2018).

The k_1 of PFO was found to be 0.073 and 0.115 min^{-1} for Fe_3O_4 nanoparticles and Fe_3O_4/NiO composite, respectively. While the k_2 of PSO was determined to be 0.00102 and 0.0013 $g\ mg^{-1}\ min^{-1}$ for Fe_3O_4 nanoparticles and Fe_3O_4/NiO composite, respectively.

For Cr(VI) ions, the R^2 values obtained from the PSO model were 0.988 and 0.976, while those obtained from the PFO model were 0.876 and 0.805 for Fe_3O_4 nanoparticles and Fe_3O_4/NiO composite, respectively. The best-fitting model for the adsorption process was PSO, according to R^2 analysis. Table 3 shows the corresponding kinetic parameters. These results also revealed that the as-prepared adsorbents' adsorption kinetics may be adequately explained by the PSO model, indicating that chemical adsorption is the step that determines rate. The observations reveal that adsorption happens via chemical interactions (chemisorption) and the availability of adsorption sites. The Cr(VI) adsorption by Fe_3O_4 nanoparticles and Fe_3O_4/NiO composite was thus investigated using a PSO model.

3.8 Adsorption Isotherm

Adsorption isotherm is a key consideration in the development of adsorption systems and is frequently employed for the evaluation of the adsorption capacity (Li et al., 2021). It is also used to describe the interaction between the adsorbate and the adsorbent. The adsorption capacity of Fe_3O_4 nanoparticles and
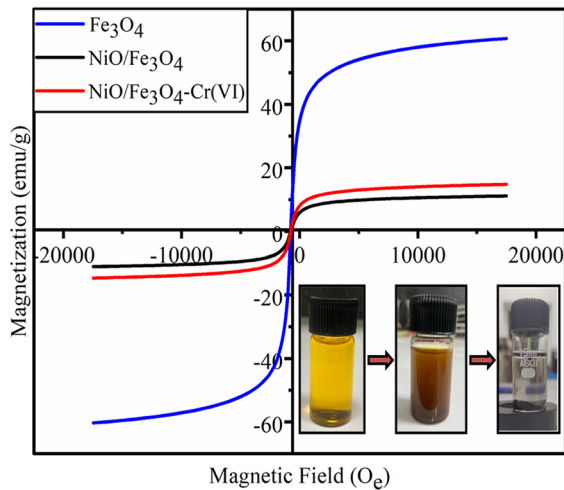
Fig. 7 Magnetization curves of the Fe_3O_4 nanoparticle, Fe_3O_4/NiO composite, and Fe_3O_4/NiO composite after Cr(VI) adsorption

Fe_3O_4/NiO composite was estimated using isotherm models, including Langmuir, Freundlich, Temkin, Harkins–Jura, Hasley, and Redlich and Peterson (Saraswat et al., 2020).

In order to depict monomolecular layer adsorption, the Langmuir isotherm model presupposes that the adsorption takes place on a homogenous surface and that there is no interaction between adsorbate molecules. Linearized forms of the Langmuir isotherm are represented as

$$\text{Langmuir type 1}\quad \frac{C_e}{q_e} = \frac{1}{K_L q_m} + \frac{C_e}{q_m} \tag{5}$$

where K_L is the Langmuir adsorption equilibrium constant.

The parameters were obtained by plotting C_e/q_e vs C_e, $1/q_e$ vs $1/C_e$, and q_e vs q_e/C_e (Figs. 10 and 11) (Raghav & Kumar, 2019). The values of q_m and other Langmuir parameters are shown in Table 3. For Fe_3O_4 nanoparticles and the Fe_3O_4/NiO composite, the q_m value determined by the Langmuir type 1 isotherm was 96.15 mg g^{-1} and 150 mg g^{-1}, respectively. Among the three types of Langmuir isotherms, Langmuir type 1 is best suited for the process of adsorption.

The Freundlich adsorption model presupposes that the surfaces of the adsorbents are heterogeneous and contain sites with various adsorption potentials. Furthermore, it is hypothesized that stronger binding sites are used first and that binding strength decreases as occupancy rises (Gayathri et al., 2021). The linearized form is represented as
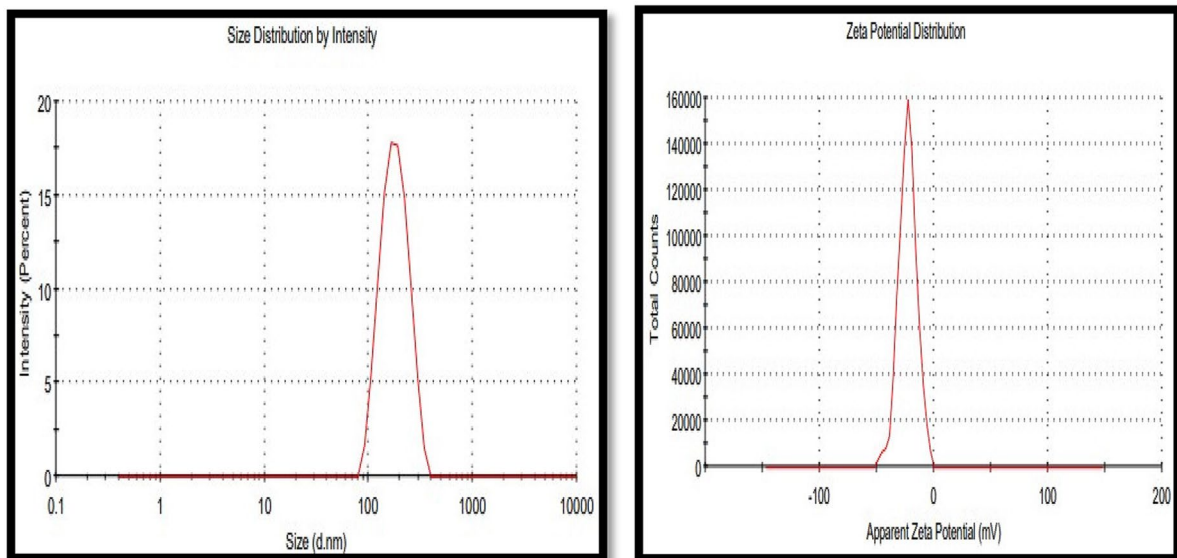
$$\ln q_e = \ln K_F + \frac{1}{n} \ln C_e \tag{6}$$

Fig. 8 **a** Particle size distribution of Fe_3O_4 nanoparticles and **b** zeta potential of Fe_3O_4 nanoparticles
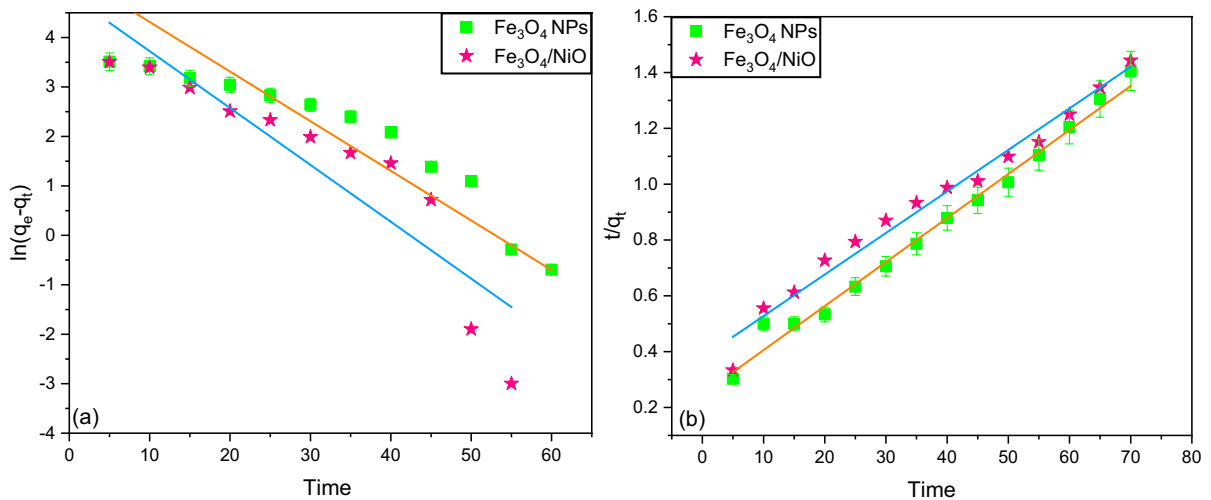
Fig. 9 **a** PFO and **b** PSO for Fe$_3$O$_4$ nanoparticles and Fe$_3$O$_4$/NiO composite

where K_F is the Freundlich constant and n is the adsorption intensity, indicating favorable or unfavorable adsorption processes. The parameters were obtained by plotting $\ln q_e$ vs $\ln C_e$ (Fig. 12a). The Freundlich isotherm becomes linear at $n = 1$ and shows that the adsorption affinities of all the sites on the Fe$_3$O$_4$ nanoparticles and the Fe$_3$O$_4$/NiO composite are equal. Adsorption intensity ($n > 1$) shows that affinity decreases as adsorption density increases, whereas $n < 1$ shows poor adsorption. For the Cr(VI) adsorption process, the adsorption intensity (n) values were 1.92 and 1.96 for Fe$_3$O$_4$ nanoparticles and Fe$_3$O$_4$/NiO

composite which are larger than 1, indicating favorable adsorption. Good adsorption is indicated by the Freundlich isotherm constant value of $1/n$, which is between 0 and 1. The K_F and $1/n$ values were determined to be 140.54 and 0.522 for Fe$_3$O$_4$ nanoparticles and 179.82 and 0.51 for Fe$_3$O$_4$/NiO composite, respectively. The R^2 value of Freundlich model was found to be 0.692 and 0.875 for Fe$_3$O$_4$ nanoparticles and Fe$_3$O$_4$/NiO composite.

According to the Temkin isotherm, the adsorption energy decreases linearly rather than logarithmically. This isotherm is known for describing how adsorbate and adsorbent interact (Azizkhani et al., 2021). The isotherm is given by the equation

$$q_e = \frac{RT}{b_T} \ln (K_T C_e) \tag{7}$$

$$q_e = B_T \ln (K_T C_e) \tag{8}$$

where $B_T = \frac{RT}{b_T}$

where B_T is the heat of adsorption, the Temkin isotherm constant, or b_T, measures the change in adsorption energy, and K_T is the equilibrium binding constant. Figure 12b shows the Temkin isotherm, and the values of B_T were 28.69 and 19.84 J mol^{-1} for Fe$_3$O$_4$ nanoparticles and Fe$_3$O$_4$/NiO composite, respectively. The values of K_T are 0.061 and 0.237 L mg^{-1} for Fe$_3$O$_4$ nanoparticles and Fe$_3$O$_4$/NiO composite, respectively. The R^2 value of

Table 3 Kinetic parameters of Fe$_3$O$_4$ nanoparticle and Fe$_3$O$_4$/NiO composite

Adsorbent	Kinetic models	Parameters	Values
Fe$_3$O$_4$	PFO	k_1 (min^{-1})	0.073
		q_e (mg/g)	84.41
		R^2	0.876
	PSO	k_2 (g/mg/ min)	0.00102
		q_e (mg/g)	62.81
		R^2	0.988
Fe$_3$O$_4$/NiO	PFO	k_1 (min^{-1})	0.115
		q_e (mg/g)	130.82
		R^2	0.805
	PSO	k_2 (g/mg/ min)	0.0013
		q_e (mg/g)	67.20
		R^2	0.976

Fig. 10 Different types of Langmuir plots for Fe_3O_4 nanoparticle (**a**–**c**)
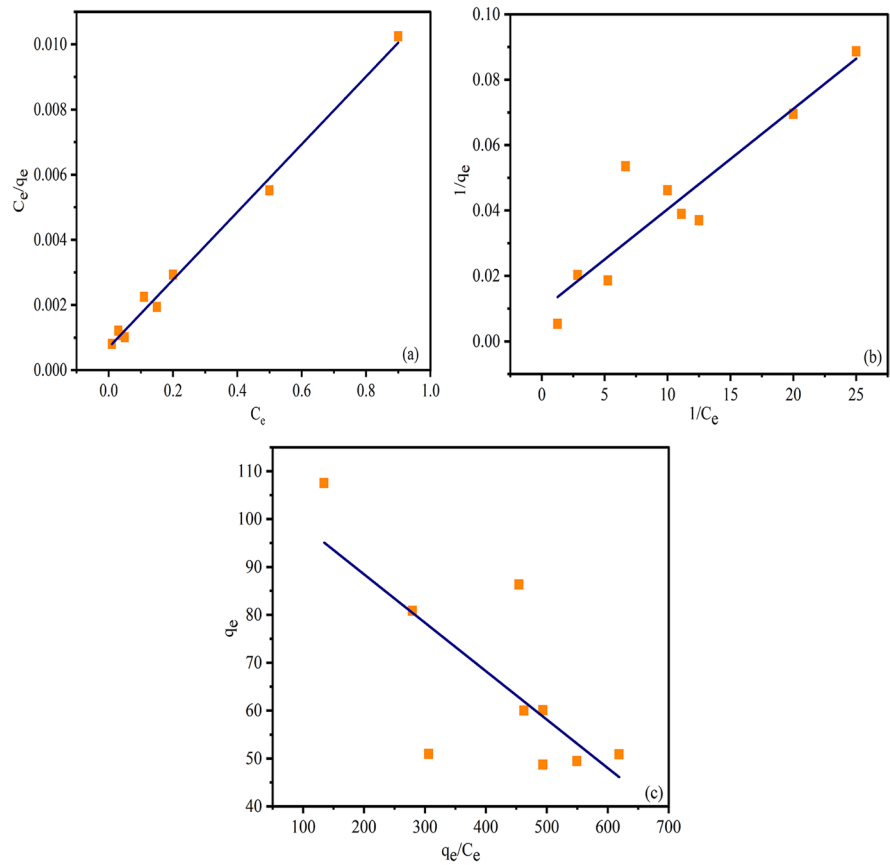
Temkin model was found to be 0.893 and 0.631 for Fe_3O_4 nanoparticles and Fe_3O_4/NiO composite.

According to the Harkins–Jura model, which focuses on multilayer adsorption and the existence of heterogeneous pore distribution on adsorbent surfaces (Khan et al., 2022), this can be defined as

$$\frac{1}{q_e^2} = \frac{B_{HJ}}{A_{HJ}} - \frac{1}{A_{HJ}}\log(C_e) \tag{9}$$

where B_{HJ} and A_{HJ} are the Harkins–Jura constant. The slope and intercept of the linear plot based on $1/q_e^2$ vs $\log(C_e)$ can be used to determine B_{HJ} and A_{HJ}. Figure 12 c shows the Harkins–Jura model for Cr(VI) removal on both adsorbents, and Table 4 summarizes the required isotherm parameters. The R^2 value of Harkins–Jura model was found to be 0.425 and 0.325 for Fe_3O_4 nanoparticles and Fe_3O_4/NiO composite.

Additionally, multilayer adsorption at a comparatively great distance from the surface was assessed using the Hasley isotherm model (Buema et al., 2021). The adsorption isotherm can be written as

$$\ln q_e = \frac{1}{n_H}\ln K_H - \frac{1}{n_H}\ln\frac{1}{C_e} \tag{10}$$

where K_H and n_H are the Hasley constants, which can be calculated from the slope and the intercept of the linear plot based on $\ln(q_e)$ vs $\ln(1/C_e)$. Figure 12 d shows the Hasley isotherm model for Cr(VI) removal. The R^2 value of Hasley model was found to be 0.692 and 0.674 for Fe_3O_4 nanoparticles and Fe_3O_4/NiO composite.

The Freundlich and Langmuir isotherms are part of the three-parameter Redlich-Peterson empirical adsorption model (Naik et al., 2023). The isotherm has the following linear form

$$\ln\frac{C_e}{q_e} = B\ln C_e - \ln A \tag{11}$$

Fig. 11 Different types of Langmuir plots for Fe$_3$O$_4$/NiO composite (**a**–**c**)
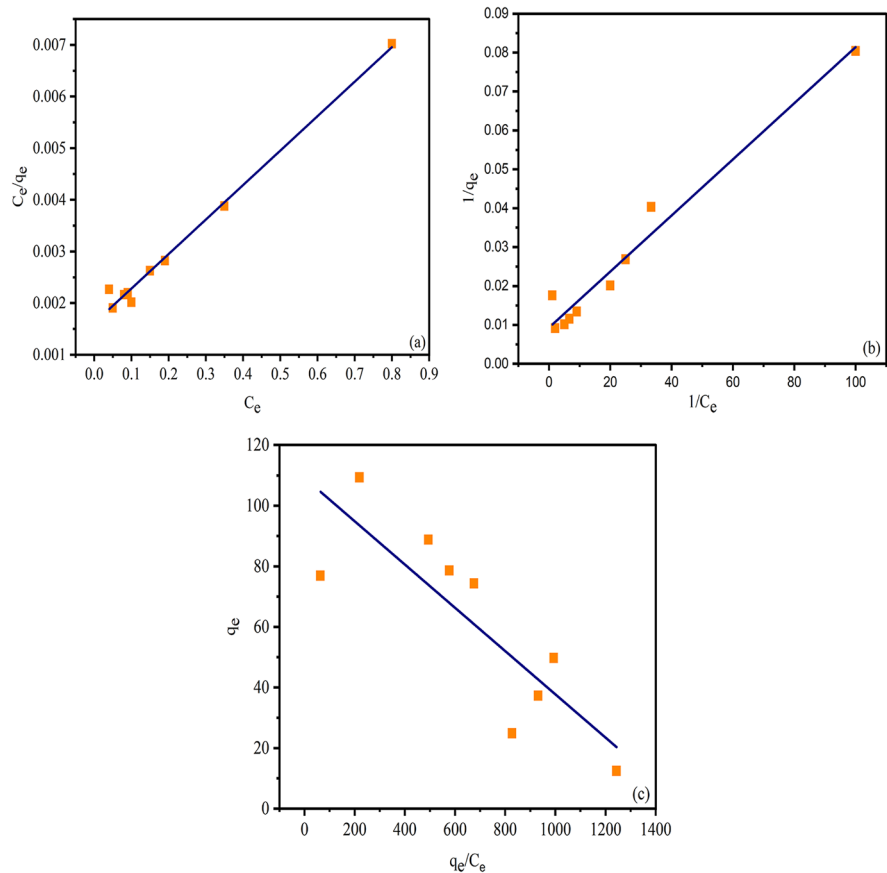
where A (L g^{-1}) and B (L mg^{-1}) are the Redlich-Peterson isotherm constants. Figure 12 e illustrates the plot of ln(C_e/q_e) against lnC_e. The values of the Redlich-Peterson isotherm constants are presented in Table 4. The R^2 value of Redlich-Peterson was found to be 0.950 and 0.977 for Fe$_3$O$_4$ nanoparticles and Fe$_3$O$_4$/NiO composite.

3.9 Thermodynamic Study

Thermodynamic parameters were calculated in order to analyze the thermodynamics of the adsorption of Cr(VI) ions onto Fe$_3$O$_4$ nanoparticles and Fe$_3$O$_4$/NiO composite. The ΔG denotes the spontaneity of the adsorption process. ΔH determines whether the sorption process is endothermic or exothermic. The following equations were used to determine the thermodynamic parameters.
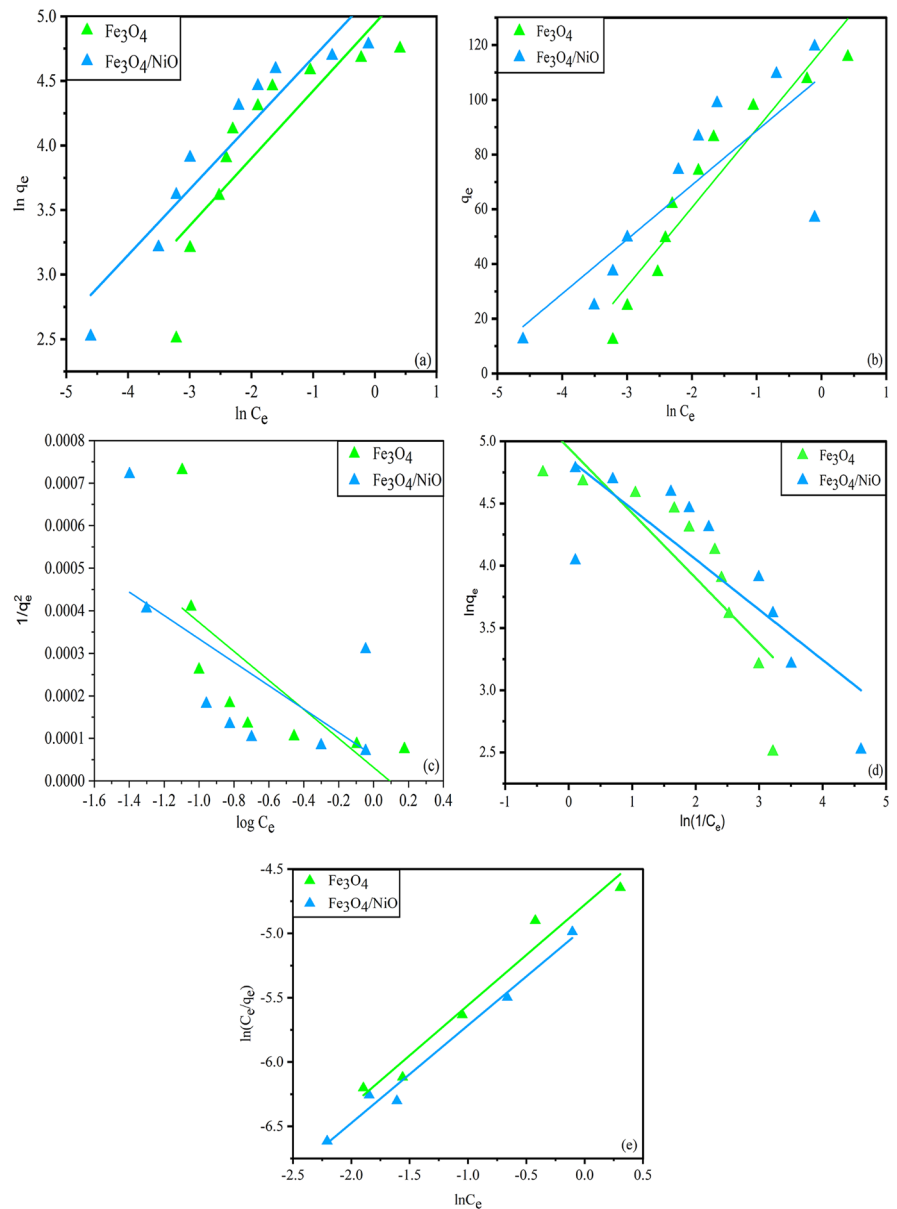
$$\ln C_e = -\ln K_o + \Delta H/RT \tag{12}$$

$$\Delta G = \Delta H - T\Delta S \tag{13}$$

Using the above equation, the plot of ln C_e vs $1/T$ is shown in Fig. 12 (Raghav & Kumar, 2018). Table 5 shows the thermodynamic parameters for Cr(VI) adsorption on both the adsorbents. The calculated ΔG values were as follows: -56.74, -58.61, and -60.49 kJ mol^{-1} for Fe$_3$O$_4$ nanoparticles and -57.43, -59.32, and -61.22 kJ mol^{-1} for Fe$_3$O$_4$/NiO composite at 303 K, 313 K, and 323 K, respectively. The negative values of ΔG demonstrated that the sorption process of Cr(VI) by adsorbents was feasible and spontaneous. The negative ΔH values of -59.27 and -61.31 kJ mol^{-1} for Fe$_3$O$_4$ nanoparticles and Fe$_3$O$_4$/NiO composite, respectively, proved the exothermic nature of the process.

Furthermore, positive ΔS values suggested that the adsorbent surface had an affinity for the Cr(VI) ion and that the degrees of disorder and randomness

Fig. 12 **a** Freundlich, **b** Temkin, **c** Harkins–Jura, **d** Hasley, **e** Redlich-Peterson isotherm plots for Fe_3O_4 nanoparticles and Fe_3O_4/NiO composite

3.10 Variation of Adsorbent Dose

The dosage of the adsorbent is a crucial functional component that significantly affects the removal efficiency and adsorption capacity. It is critical to assess the effectiveness and efficiency of the adsorption process. The adsorbent dosage should show high removal efficiency and a suitable capacity to adsorb. Figure 14 depicts the influence of adsorbent dose on percentage removal and adsorption capacity of Cr(VI). As is well known, upon increasing Fe_3O_4 nanoparticle dosage from 0.01 to 0.14 g L^{-1}, a reduction in adsorption capacity from 125 to 17.75 mg g^{-1} occurs while improving removal efficiency from 50 to 99.4%. Also, adsorption capacity decreases from 147.5 to 17.786 mg g^{-1}, and removal efficiency increases from 59 to 99.6% for Fe_3O_4/NiO as dosage increases from 0.01 to 0.14 g L^{-1}. On increasing the adsorbent's dosage, the

at the solid-solution interface were high in show in Fig. 13.

Table 4 Isotherm parameters of Fe_3O_4 nanoparticles and Fe_3O_4/NiO composite

Adsorbent	Adsorption isotherm	Parameters	Values
Fe_3O_4	Langmuir type 1	q_m (mg/g)	96.15
		K_L (L/mg)	0.014
		R_L	0.003
		R^2	0.991
	Langmuir type 2	q_m (mg/g)	103
		K_L (L/mg)	0.003
		R_L	0.015
		R^2	0.821
	Langmuir type 3	q_m (mg/g)	98.02
		K_L (L/mg)	0.0098
		R_L	0.005
		R^2	0.48
	Freundlich	K_F	140.54
		n	1.92
		$1/n$	0.522
		R^2	0.692
	Temkin	b_T (kJ/mol)	0.089
		B_T (J/mol)	28.69
		K_T (L/mg)	0.061
		R^2	0.893
	Harkins–Jura	A_{HJ}	2930
		B_{HJ}	0.094
		R^2	0.425
	Hasley	K_H	13.006
		n_H	1.916
		R^2	0.692
	Redlich-Peterson	B	0.781
		A	118.77
		R^2	0.950

Table 4 (continued)

Adsorbent	Adsorption isotherm	Parameters	Values
Fe_3O_4/NiO	Langmuir type 1	q_m (mg/g)	150
		K_L (L/mg)	0.004
		R_L	0.012
		R^2	0.987
	Langmuir type 2	q_m (mg/g)	107
		K_L (L/mg)	0.012
		R_L	0.0038
		R^2	0.961
	Langmuir type 3	q_m (mg/g)	103.26
		K_L (L/mg)	0.014
		R_L	0.0035
		R^2	0.666
	Freundlich	K_F	179.82
		n	1.96
		$1/n$	0.51
		R^2	0.875
	Temkin	b_T (kJ/mol)	0.127
		B_T (J/mol)	19.84
		K_T (L/mg)	0.237
		R^2	0.631
	Harkins–Jura	A_{HJ}	3640
		B_{HJ}	0.215
		R^2	0.325
	Hasley	K_H	167.55
		n_H	2.475
		R^2	0.674
	Redlich-Peterson	B	0.759
		A	141.837
		R^2	0.977

number of unsaturated sites in the process increases, or the agglomeration of Fe_3O_4 nanoparticles and Fe_3O_4/NiO composite results in a reduction in the accessible surface area and the adsorption capacity (Nodehi et al., 2022).

3.11 Variation of pH

Particularly, compared to Fe_3O_4 nanoparticles, Fe_3O_4/NiO composite had greater Cr(VI) removal efficiency. As can be seen in Fig. 15a, a pH range of 4 to 9 was used to investigate the effect of pH on the ability of Fe_3O_4 nanoparticles and Fe_3O_4/NiO composite to remove Cr(VI). For both adsorbents, the greatest

Cr(VI) removal efficiency was noted at pH 5. As demonstrated in Fig. 15a, in a pH range of 4 to 5, the % adsorption increases, while a further increase in pH up to 9 results in a dramatic decrease in % adsorption. The percentage adsorption for Cr(VI) reached 90% and 94.5% for Fe_3O_4 nanoparticles and Fe_3O_4/NiO composite at pH = 5. Generally, chromium exists

Table 5 The thermodynamic parameters of Fe$_3$O$_4$ nanoparticles and Fe$_3$O$_4$/NiO composite

| Adsorbent	R^2	ΔH (kJ mol^{-1})	ΔS (J mol^{-1} K^{-1})	ΔG (kJ mol^{-1})		
				303 K	313 K	323 K
Fe$_3$O$_4$	0.99281	-59.27	187.09	-56.74	-58.61	-60.49
Fe$_3$O$_4$/NiO	0.97719	-61.31	189.35	-57.43	-59.32	-61.22
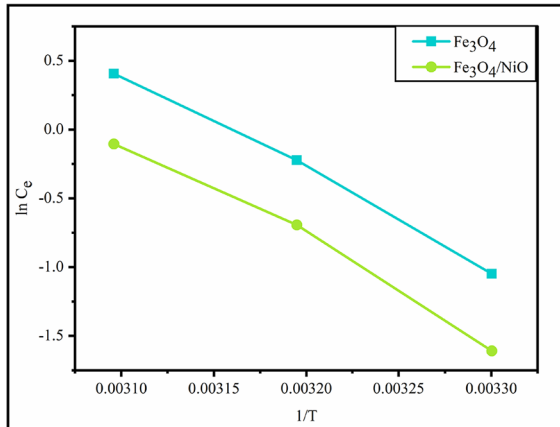
Fig. 13 Linear dependence of ln(C_e) on $1/T$ based on adsorption thermodynamics for Fe$_3$O$_4$ nanoparticles and Fe$_3$O$_4$/NiO composite

in the pH range of 1–6 in the form of HCrO$_4^-$, followed by CrO$_4^{2-}$ and Cr$_2$O$_7^{2-}$ ions. In an acidic environment, the adsorbent surface was protonated with

H$^+$ ions, which facilitated the electrostatic attraction of Cr(VI) ions in the form of HCrO$_4^-$ ions to the positively charged adsorbent surface. When the pH is increased, the surface of both adsorbents becomes less positively charged, reducing electrostatic attractions between the adsorbent surface and negatively charged species and thereby lowering adsorption efficiency. With increasing solution pH, the competition of OH$^-$ for the few adsorption sites became more intense. As a result, pH 5 was chosen as the most suitable condition in this study. Hence, all subsequent adsorption tests were carried out at pH 5 to achieve maximum removal of Cr(VI) onto both adsorbents (Kang et al., 2022).

3.12 Variation of Contact Time

Another aspect that influences adsorption capacity is contact time. The equilibrium adsorption contact time and the rate at which it is reached are two important characteristics of adsorption. To assess the
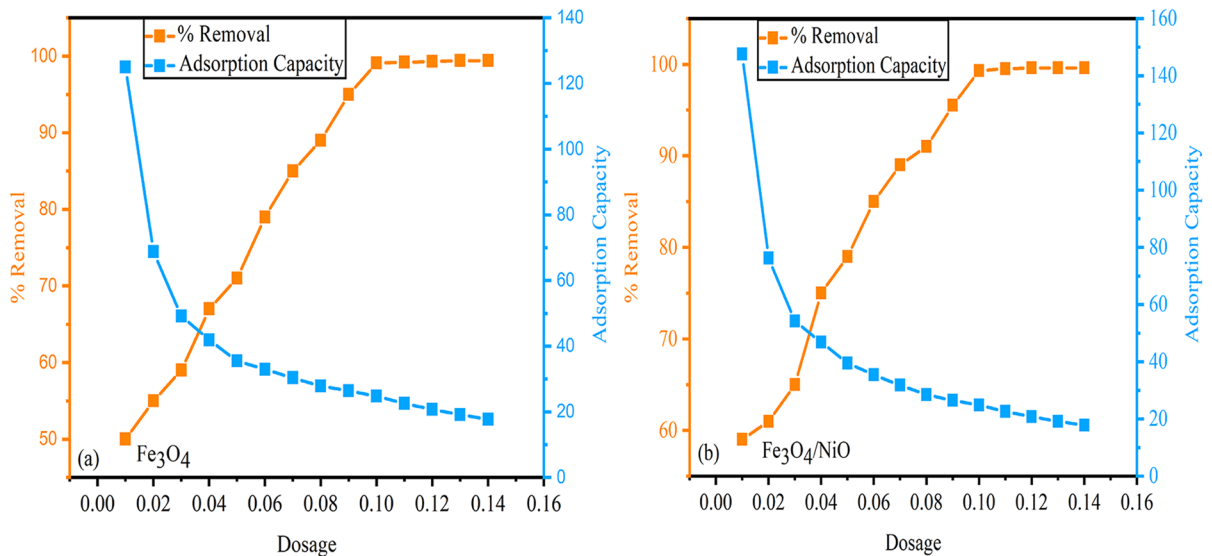
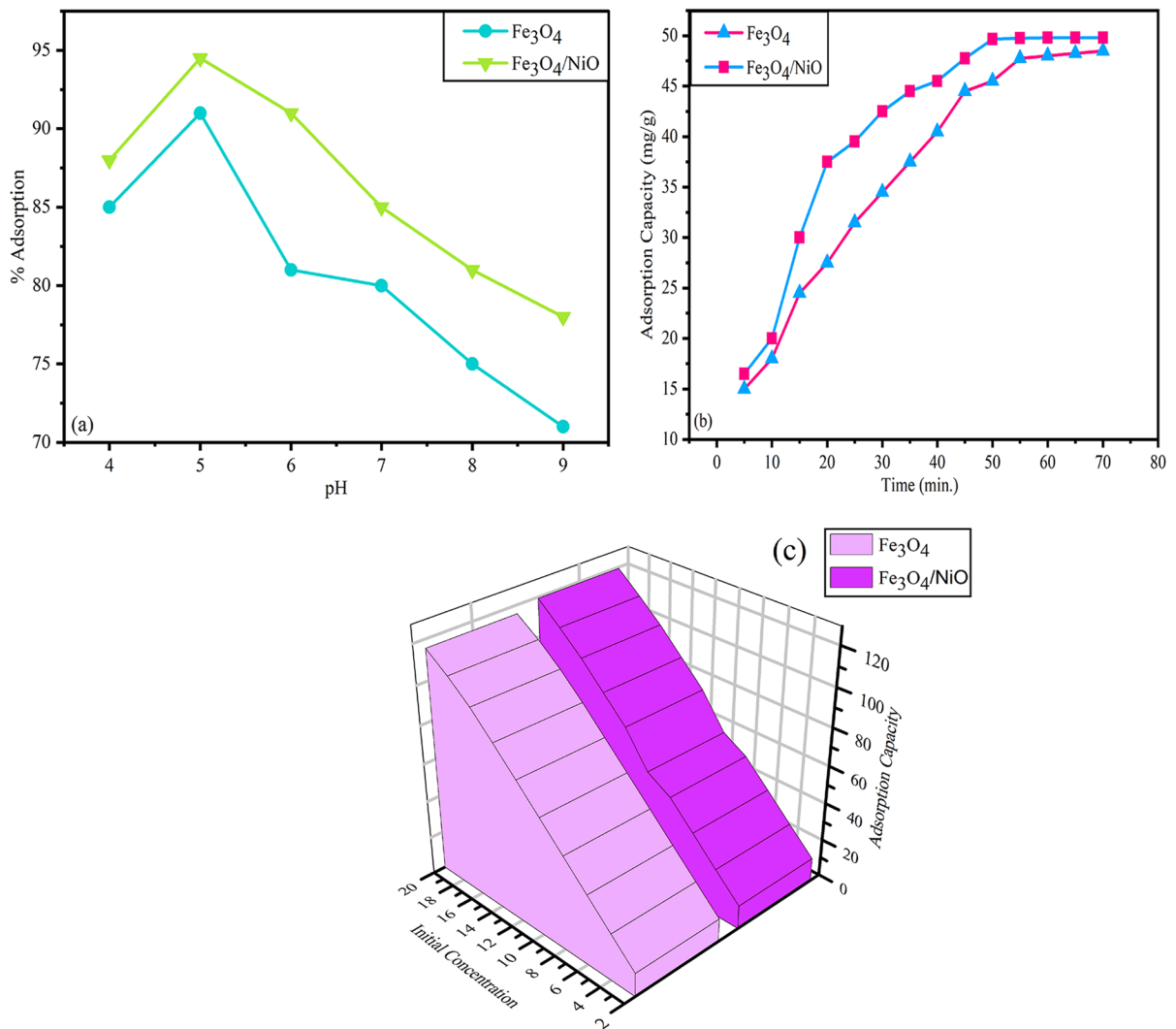**Fig. 14** Variation of adsorbent dose **a** Fe$_3$O$_4$ nanoparticles and **b** Fe$_3$O$_4$/NiO composite

Fig. 15 Variation of **a** pH, **b** contact time, and **c** initial concentration

Cr(VI) adsorption behavior by Fe_3O_4 nanoparticles and Fe_3O_4/NiO composite, the effect of contact time between the adsorbent and adsorbate was optimized in this work by altering the contact duration from 5 to 70 min (Fig. 15b). At 60 min, the maximal adsorption capacity occurs, demonstrating fast adsorption at the start of the adsorption. The capacity of adsorption reached 48 mg g^{-1} and 49.8 mg g^{-1} for Fe_3O_4 nanoparticles and Fe_3O_4/NiO composite in the first 60 min of the process, respectively. After achieving equilibrium, increasing the contact time had no further influence on sorption. The remaining ions in solution have a harder time diffusing to and interacting with the adsorbent as time goes on because the adsorbent sites are gradually filled up. The huge surface area accessible for Cr(VI) adsorption causes rapid adsorption at the start of the contact time. According to the findings, the equilibrium time for the elimination of Cr(VI) was 60 min (Nodehi et al., 2022).

3.13 Variation of Initial Concentration

Initial concentration variations are one of the most important criteria for optimizing the related values between contaminants in aqueous media and

adsorbents in equilibrium studies. The effect of initial Cr(VI) concentration on the adsorption capacity of Fe_3O_4 nanoparticles and Fe_3O_4/NiO composite was examined at concentrations varying from 2 to 20 mg L^{-1}. Figure 15 c illustrates how the Cr(VI) adsorption capacity increases from 12.25 to 115.625 mg g^{-1} and 12.4375 to 119.375 mg g^{-1} for Fe_3O_4 nanoparticles and Fe_3O_4/NiO composite, respectively, as the starting solution concentration rises from 2 to 20 mg L^{-1} (Koohi et al., 2021). As the concentration of Cr(VI) increases above the previously indicated threshold, the active adsorbent sites are rapidly occupied. Hence, the adsorbent is unable to absorb any further Cr(VI) values. The saturation of the adsorbent surface inhibits further adsorption (Mahmoudi & Behnajady, 2018). At initial concentration of 10 mg L^{-1}, maximum percentage removal and sufficient adsorption capacity were observed for Fe_3O_4 nanoparticles and Fe_3O_4/NiO composite. Therefore, 10 mg L^{-1} was chosen as an optimal adsorbate concentration for study of both the adsorbents.

3.14 Comparative Study

In Table 6 study the comparative study the relative adsorption capacity of different adsorbents for removal of Cr(VI).

3.15 Regeneration Studies

It is highly beneficial to conduct researches on the rate of desorption and the capacity to recover adsorbent during the reuse of regenerated adsorbents. Additionally, adsorbent regeneration research is crucial for environmental considerations in addition to economic ones. Figure 16 depicts the regeneration and reuse performance of Fe_3O_4 nanoparticles and Fe_3O_4/NiO composites over six successive adsorption–desorption experiment cycles. For this work, NaOH solution (0.1 M) was used as the desorption medium. Fe_3O_4 nanoparticles and Fe_3O_4/NiO composite after the experiment were stirred continuously for 30 min in NaOH solution. After six cycles, the percentage removal of Cr(VI) by Fe_3O_4 nanoparticles and Fe_3O_4/NiO composite was reduced from 97 to 54% and 98.45 to 71%, respectively. That could be explained by the fact that not all of the Cr(VI) molecules that had been previously adsorbed during the regeneration process were really desorbed. Our findings demonstrated that Fe_3O_4 nanoparticles and Fe_3O_4/NiO composites are promising materials for the elimination of Cr(VI) from a reusability perspective since they can be rapidly regenerated by NaOH eluting treatment and reutilized well in the following cycle (Koohi et al., 2021).

Table 6 The relative adsorption capacity of different adsorbents for removal of Cr (VI)

| S. no	Materials	Q_e (mg/g)	References
1	Fe_3O_4/C nanocomposites	64.0	Su et al., (2019)
2	Fe_3O_4/graphene oxide (GO)/clay composite	71.47	Esmaeili & Tamjidi, (2020)
3	Chitosan@Fe_3O_4	16.94	Sanchayanukun & Muncharoen, (2019)
4	g-C_3N_4/Fe_3O_4 nanocomposites	59.2	Duan et al., (2019)
5	Graphene oxide-magnetic composite	3.197	Neolaka., (2020)
6	Core–shell Fe_3O_4@Ce-Zr binary oxide	66.7	Yu & Fu, (2020)
7	Magnetic greigite/biochar composite	23.25	Wang et al., (2020)
8	Magnetic biochar nanocomposites	80.96	Santhosh et al., (2020)
9	Fe_3O_4-coated nanofibers based on cellulose acetate	193.2	Karamipour et al., (2020)
10	Magnetic composite functionalized with 3-aminopropyl triethoxysilane	64.92	Nnadozie & Ajibade, (2020)
11	Fe_3O_4 nanoparticle	96.15	This work
12	Fe_3O_4/NiO composite	150	This work
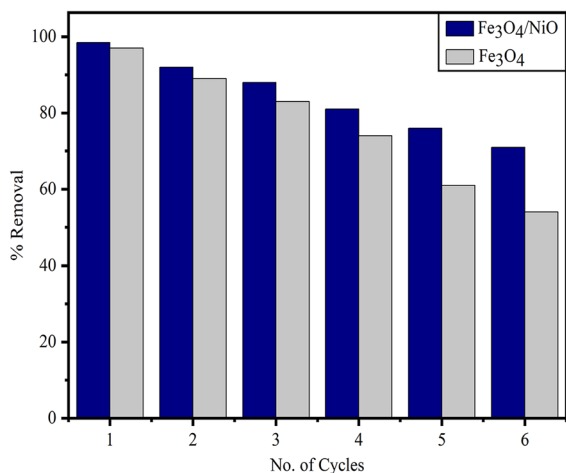
Fig. 16 Regeneration studies of Fe_3O_4 nanoparticle and Fe_3O_4/NiO composite

3.16 Mechanism

The pH values affect the different forms of chromium that are present in solutions. In acidic solutions, Fe_3O_4/NiO was protonated and had a positively charged surface. The primary forms that were present were $Cr_2O_7^{2-}$ and $HCrO_4^{-}$. Consequently, electrostatic interactions between the positively charged surface and chromate anions served as the primary adsorption processes of Cr(VI).After adsorption, FTIR was also used to describe Fe_3O_4 nanoparticle and Fe_3O_4/NiO composite. Moreover, a minor shift in the peak's position from 3401 to 3408 cm^{-1} for Fe_3O_4 nanoparticle and 3491 to 3497 cm^{-1} could be seen for Fe_3O_4/NiO composite, showing an electrostatic interaction between the Cr(VI) and the adsorbent. These were most likely caused by the electrostatic interactions ($Fe–OH_2^{+}\ldots HCrO_4^{-}$), according to earlier studies (Miao et al., 2021; Sirajudheen et al., 2020; Yang et al., 2020).

3.17 Cost Analysis

Cost-effectiveness is a key consideration for adsorbents utilized in the industry. Fe_3O_4 nanoparticles and Fe_3O_4/NiO composites were prepared using the chemicals of analytical reagent grade. Both the dry Fe_3O_4 nanoparticles and the Fe_3O_4/NiO composite are currently expensive in the lab, costing roughly US $110.00 and $149.07 per kg, respectively. However, the cost of Cr(VI) adsorption on both adsorbents is

reasonable when compared to more conventional adsorbents. It is anticipated that in the future, industrial-grade raw materials intended for commercial applications would take the place of analytical-grade compounds in the large-scale synthesis of adsorbents. As a result, the price of the adsorbents and their use will go down significantly (Soni et al., 2020b).

4 Conclusion and Future Perspective

Effective adsorbents are essential, as evidenced by the rise in water scarcity and the requirement for water treatment. Presently, contaminated water is treated using magnetic nanoparticles and their composites that have been tailored in terms of size, content, magnetic properties, and structure. Fe_3O_4 nanoparticles and Fe_3O_4/NiO composite have been successfully synthesized and used as promising sorbents for Cr(VI) adsorption. Adsorption variables such as dose, contact time, initial concentration, and pH were all taken into account and optimized. The prepared adsorbents were comprehensively characterized by various techniques to understand the surface parameters and physical properties necessary for good adsorption. The results were successfully described by the Langmuir isotherm model, which demonstrated monolayer coverage with a chemisorption-type adsorption mechanism. The utmost adsorption capacities of the Fe_3O_4 nanoparticles and Fe_3O_4/NiO composite were 96.15 mg g^{-1} and 150 mg g^{-1}, respectively. The R_L results also demonstrated that adsorption is feasible. The kinetic modeling revealed that the experimental findings fit well with the PSO model. Following adsorption, an external magnetic field was employed to remove the adsorbents from the aqueous medium, and six adsorption/desorption cycle experiments demonstrated that Cr(VI) adsorbents were exceptionally reusable. As a result of these findings, it is possible to conclude that the developed Fe_3O_4 nanoparticle and Fe_3O_4/NiO composite can be used as a low-cost, easily available precursor with good reusability, easy separation, and high efficiency as an adsorbent to remove chromium from wastewater.

The following are our major conclusions and future perspectives:

(1) Fe_3O_4 nanoparticles and their composites have the advantages of being inexpensive, tunable, and

having outstanding magnetic properties as adsorbents.

(2) In comparison to other adsorbents that have been previously described, Fe_3O_4 nanoparticles and their composites exhibit a larger sorption capacity and a fast sorption rate.

(3) The adsorption properties of Fe_3O_4 nanoparticles and their composites are influenced by various factors, including surface area, surface charge, annealing temperature, functional groups, and cation distribution.

(4) Regeneration of these adsorbents can be accomplished by using low concentrations of acids or bases or by adjusting the pH of the solution. Furthermore, consistent adsorption–desorption patterns have been noted after multiple regeneration cycles.

(5) A broad pH range is required for Fe_3O_4 nanoparticles and their composites to function in real-world scenarios.

(6) Comparing magnetic adsorbents to various new generation adsorbents, an additional benefit is their simple sorption-magnetic separation-regeneration properties, which speed up the cyclic and repeated use of magnetic adsorbents over extended periods of time.

(7) Prior to being used as either catalysts that promote organic processes or for the breakdown of organic pollutants, more research is required on pollutant-loaded magnetic sorbents.

Data Availability The data used to support the findings of this study are available from the corresponding author upon request.

Declarations

Competing Interests The authors declare no competing interests.

References

Abbas, A., & Hussain, M. A. (2016). Design, characterization and evaluation of. *PLoS ONE, 11*, 0151367.

Abbas, A., Hussain, M. A., Amin, M., Sher, M., Tahir, M. N., & Tremel, W. (2015). Succinate-bonded pullulan: An efficient and reusable super-sorbent for cadmium-uptake from spiked high-hardness groundwater. *Journal of Environmental Sciences, 37*, 51.

Abdullah, N. H., Shameli, K., Abdullah, E. C., & Abdullah, L. C. (2019). Solid matrices for fabrication of magnetic iron oxide nanocomposites: Synthesis, properties, and application for the adsorption of heavy metal ions and dyes. *Composites Part B: Engineering, 162*, 538–568.

Abegunde, S. M., Idowu, K. S., Adejuwon, O. M., & Adeyemi-Adejolu, T. (2020). A review on the influence of chemical modification on the performance of adsorbents. *Resources, Environment and Sustainability, 1*, 100001.

Almomani, F., & Bhosale, R. R. (2021). Bio-sorption of toxic metals from industrial wastewater by algae strains Spirulina platensis and Chlorella vulgaris: Application of isotherm, kinetic models and process optimization. *Science of the Total Environment, 755*, 142654.

Arora, C., Soni, S., Sahu, S., Mittal, J., Kumar, P., & Bajpai, P. K. (2019). Iron based metal organic framework for efficient removal of methylene blue dye from industrial waste. *Journal of Molecular Liquids, 284*, 343.

Ashan, S. K., Ziaeifar, N., & Khalilnezhad, R. (2018). Artificial neural network modelling of Cr (VI) surface adsorption with NiO nanoparticles using the results obtained from optimization of response surface methodology. *Neural Computing and Applications, 29*, 969–979.

Azizkhani, S., Hussain, S. A., Abdullah, N., Ismail, M. H. S., & Mohammad, A. W. (2021). Synthesis and application of functionalized Graphene oxide-silica with chitosan for removal of Cd (II) from aqueous solution. *Journal of Environmental Health Science and Engineering, 19*, 491–502.

Bin-Dahman, O. A., & Saleh, T. A. (2024). Synthesis of polyamide grafted on bio support as polymeric adsorbents for the removal of dye and metal ions. *Biomass Conversion and Biorefinery, 14*, 2439–2452.

Buema, G., Lupu, N., Chiriac, H., Ciobanu, G., Bucur, R. D., Bucur, D., Favier, L., & Harja, M. (2021). Performance assessment of five adsorbents based on fly ash for removal of cadmium ions. *Journal of Molecular Liquids, 333*, 115932.

Chaki, S. H., Malek, T. J., Chaudhary, M. D., Tailor, J. P., & Deshpande, M. P. (2015). Magnetite Fe_3O_4 nanoparticles synthesis by wet chemical reduction and their characterization. *Advances in Natural Sciences: Nanoscience and Nanotechnology, 6*, 035009.

Duan, J., Zhao, L., Lv, W., Li, Y., Zhang, Y., Ai, S., & Zhu, L. (2019). Facile synthesis of g-C_3N_4/Fe_3O_4 nanocomposites for fluorescent detection and removal of Cr (VI). *Microchemical Journal, 150*, 104105.

Eltaweil, A. S., El-Monaem, E. M. A., Mohy-Eldin, M. S., & Omer, A. M. (2021). Fabrication of attapulgite/magnetic aminated chitosan composite as efficient and reusable adsorbent for Cr (VI) ions. *Scientific Reports, 11*, 16598.

Esmaeili, H., & Tamjidi, S. (2020). Ultrasonic-assisted synthesis of natural clay/Fe_3O_4/graphene oxide for enhances removal of Cr (VI) from aqueous media. *Environmental Science and Pollution Research, 27*, 31652–31664.

Gayathri, R., Gopinath, K. P., & Kumar, P. S. (2021). Adsorptive separation of toxic metals from aquatic environment

using agro waste biochar: Application in electroplating industrial wastewater. *Chemosphere, 262*, 128031.

Hassan, A. F., & Hrdina, R. (2022). Enhanced removal of arsenic from aqueous medium by modified silica nanospheres: Kinetic and thermodynamic studies. *Arabian Journal for Science and Engineering, 47*, 281–293.

Imran, M., Khan, Z. U. H., Iqbal, M. M., Iqbal, J., Shah, N. S., Munawar, S., Ali, S., Murtaza, B., Naeem, M. A., & Rizwan, M. (2020). Effect of biochar modified with magnetite nanoparticles and HNO$_3$ for efficient removal of Cr (VI) from contaminated water: A batch and column scale study. *Environmental Pollution, 261*, 114231.

Kang, Z., Gao, H., Hu, Z., Jia, X., & Wen, D. (2022). Ni–Fe/reduced graphene oxide nanocomposites for hexavalent chromium reduction in an aqueous environment. *ACS Omega, 7*, 4041–4051.

Karamipour, A., Parsi, P. K., Zahedi, P., & Moosavian, S. M. A. (2020). Using Fe$_3$O$_4$-coated nanofibers based on cellulose acetate/chitosan for adsorption of Cr (VI), Ni (II) and phenol from aqueous solutions. *International Journal of Biological Macromolecules, 154*, 1132–1139.

Khan, Q., Zahoor, M., Salman, S. M., Wahab, M., Talha, M., Kamran, A. W., Khan, Y., Ullah, R., Ali, E. A., & Shah, A. B. (2022). The chemically modified leaves of Pteris vittata as efficient adsorbent for zinc (II) removal from aqueous solution. *Water, 14*, 4039.

Khare, N., Bajpai, J., & Bajpai, A. K. (2018). Graphene coated iron oxide (GCIO) nanoparticles as efficient adsorbent for removal of chromium ions: Preparation, characterization and batch adsorption studies. *Environmental Nanotechnology, Monitoring & Management, 10*, 148–162.

Kobielska, P. A., Howarth, A. J., Farha, O. K., & Nayak, S. (2018). Metal–organic frameworks for heavy metal removal from water. *Coordination Chemistry Reviews, 358*, 92.

Koohi, P., Rahbar-kelishami, A., & Shayesteh, H. (2021). Efficient removal of congo red dye using Fe$_3$O$_4$/NiO nanocomposite: Synthesis and characterization. *Environmental Technology & Innovation, 23*, 101559.

Li, S., Wen, N., Wei, D., & Zhang, Y. (2021). Highly effective removal of lead and cadmium ions from wastewater by bifunctional magnetic mesoporous silica. *Separation and Purification Technology, 265*, 118341.

Lodhi, B. A., Abbas, A., Hussain, M. A., Hussain, S. Z., Sher, M., & Hussain, I. (2019). Design, characterization and appraisal of chemically modified polysaccharide based mucilage from Ocimum basilicum (basil) seeds for the removal of Cd (II) from spiked high-hardness ground water. *Journal of Molecular Liquids, 274*, 15.

Mahdavi, S., & Amini, N. (2016). The role of bare and modified nano nickel oxide as efficient adsorbents for the removal of Cd^{2+}, Cu^{2+}, and Ni^{2+} from aqueous solution. *Environmental Earth Sciences, 75*, 1–15.

Mahmoudi, E., & Behnajady, M. A. (2018). Synthesis of Fe$_3$O$_4$@NiO core-shell nanocomposite by the precipitation method and investigation of Cr (VI) adsorption efficiency. *Colloids and Surfaces a: Physicochemical and Engineering Aspects, 538*, 287–296.

Manoj, S., RamyaPriya, R., & Elango, L. (2021). Long-term exposure to chromium contaminated waters and the associated human health risk in a highly contaminated industrialised region. *Environmental Science and Pollution Research, 28*, 4276.

Miao, J., Zhao, X., Zhang, Y. X., & Liu, Z. H. (2021). Feasible synthesis of hierarchical porous MgAl-borate LDHs functionalized Fe$_3$O$_4$@SiO$_2$ magnetic microspheres with excellent adsorption performance toward congo red and Cr (VI) pollutants. *Journal of Alloys and Compounds, 861*, 157974.

Mohammadi, H., Nekobahr, E., Akhtari, J., Saeedi, M., Akbari, J., & Fathi, F. (2021). Synthesis and characterization of magnetite nanoparticles by co-precipitation method coated with biocompatible compounds and evaluation of in-vitro cytotoxicity. *Toxicology Reports, 8*, 331–336.

Munkaila, S., Bentley, J., Schimmel, K., Ahamad, T., Alshehri, S. M., & Bastakoti, B. P. (2021). Polymer directed synthesis of NiO nanoflowers to remove pollutant from wastewater. *Journal of Molecular Liquids, 324*, 114676.

Naik, R. L., Kumar, M. R., & Narsaiah, T. B. (2023). Removal of heavy metals (Cu & Ni) from wastewater using rice husk and orange peel as adsorbents. *Materials Today: Proceedings, 72*, 92–98.

Neolaka, Y. A., Lawa, Y., Naat, J. N., Riwu, A. A., Iqbal, M., Darmokoesoemo, H., & Kusuma, H. S. (2020). The adsorption of Cr (VI) from water samples using graphene oxide-magnetic (GO-Fe$_3$O$_4$) synthesized from natural cellulose-based graphite (kusambi wood or Schleichera oleosa): Study of kinetics, isotherms and thermodynamics. *Journal of Materials Research and Technology, 9*, 6544–6556.

Nnadozie, E. C., & Ajibade, P. A. (2020). Adsorption, kinetic and mechanistic studies of Pb (II) and Cr (VI) ions using APTES functionalized magnetic biochar. *Microporous and Mesoporous Materials, 309*, 110573.

Nodehi, R., Shayesteh, H., & Rahbar-Kelishami, A. (2022). Fe$_3$O$_4$@NiO core–shell magnetic nanoparticle for highly efficient removal of Alizarin red S anionic dye. *International Journal of Environmental Science and Technology, 19*, 2899–2912.

Pavithra, S., Thandapani, G., Sugashini, S., Sudha, P. N., Alkhamis, H. H., Alrefaei, A. F., & Almutairi, M. H. (2021). Batch adsorption studies on surface tailored chitosan/orange peel hydrogel composite for the removal of Cr (VI) and Cu (II) ions from synthetic wastewater. *Chemosphere, 271*, 129415.

Pourmortazavi, S. M., Sahebi, H., Zandavar, H., & Mirsadeghi, S. (2019). Fabrication of Fe$_3$O$_4$ nanoparticles coated by extracted shrimp peels chitosan as sustainable adsorbents for removal of chromium contaminates from wastewater: The design of experiment. *Composites Part B: Engineering, 175*, 107130.

Raghav, S., & Kumar, D. (2018). Adsorption equilibrium, kinetics, and thermodynamic studies of fluoride adsorbed by tetrametallic oxide adsorbent. *Journal of Chemical & Engineering Data, 63*, 1682–1697.

Raghav, S., & Kumar, D. (2019). Fabrication of aluminium and iron impregnated pectin biopolymeric material for effective utilization of fluoride adsorption studies. *Groundwater for Sustainable Development, 9*, 100233.

Rahman, Z., & Singh, V. P. (2019). The relative impact of toxic heavy metals (THMs)(arsenic (As), cadmium (Cd), chromium (Cr)(VI), mercury (Hg), and lead (Pb)) on the total environment: An overview. *EnvironmeNtal Monitoring and Assessment, 191*, 1.

Sanchayanukun, P., & Muncharoen, S. (2019). Elimination of Cr (VI) in laboratory wastewater using chitosan coated magnetite nanoparticles (chitosan@Fe3O4). *Environment Asia*, *12*(2), 32–48.

Santhosh, C., Daneshvar, E., Tripathi, K. M., Baltrėnas, P., Kim, T., Baltrėnaitė, E., & Bhatnagar, A. (2020). Synthesis and characterization of magnetic biochar adsorbents for the removal of Cr (VI) and Acid orange 7 dye from aqueous solution. *Environmental Science and Pollution Research*, *27*, 32874–32887.

Saraswat, S. K., Demir, M., & Gosu, V. (2020). Adsorptive removal of heavy metals from industrial effluents using cow dung as the biosorbent: Kinetic and isotherm modeling. *Environmental Quality Management*, *30*, 51–60.

Sharma, M., Singh, J., Hazra, S., & Basu, S. (2019). Adsorption of heavy metal ions by mesoporous ZnO and TiO$_2$@ZnO monoliths: Adsorption and kinetic studies. *Microchemical Journal*, *145*, 105–112.

Shekhawat, A., Kahu, S., Saravanan, D., Pandey, S., & Jugade, R. (2022). Rational modification of chitosan biopolymer for remediation of Cr (VI) from water. *Journal of Hazardous Materials Advances*, *7*, 100123.

Shi, Y., Xing, Y., Deng, S., Zhao, B., Fu, Y., & Liu, Z. (2020). Synthesis of proanthocyanidins-functionalized Fe$_3$O$_4$ magnetic nanoparticles with high solubility for removal of heavy-metal ions. *Chemical Physics Letters*, *753*, 137600.

Sirajudheen, P., Nikitha, M. R., Karthikeyan, P., & Meenakshi, S. (2020). Perceptive removal of toxic azo dyes from water using magnetic Fe$_3$O$_4$ reinforced graphene oxide–carboxymethyl cellulose recyclable composite: Adsorption investigation of parametric studies and their mechanisms. *Surfaces and Interfaces*, *21*, 100648.

Song, J., Huang, Z., & El-Din, M. G. (2021). Adsorption of metals in oil sands process water by a biochar/iron oxide composite: Influence of the composite structure and surface functional groups. *Chemical Engineering Journal*, *421*, 129937.

Soni, S., Bajpai, P. K., Mittal, J., & Arora, C. (2020a). Utilisation of cobalt doped Iron based MOF for enhanced removal and recovery of methylene blue dye from waste water. *Journal of Molecular Liquids*, *314*, 113642.

Soni, S., Bajpai, P. K., Bharti, D., Mittal, J., & Arora, C. (2020b). Removal of crystal violet from aqueous solution using iron based metal organic framework. *Desalination and Water Treatment*, *205*, 386.

Su, Q., Lin, Z., Tian, C., Su, X., Xue, X., & Su, Z. (2019). Improved removal of Cr (VI) using Fe$_3$O$_4$/C magnetic nanocomposites derived from potassium fulvic acid. *Chemistry Select*, *4*, 13656–13662.

Suo, L., Dong, X., Gao, X., Xu, J., Huang, Z., Ye, J., Lu, X., & Zhao, L. (2019). Silica-coated magnetic graphene oxide nanocomposite based magnetic solid phase extraction of trace amounts of heavy metals in water samples prior to determination by inductively coupled plasma mass spectrometry. *Microchemical Journal*, *149*, 104039.

Tang, J., Zhao, B., Lyu, H., & Li, D. (2021). Development of a novel pyrite/biochar composite (BM-FeS$_2$@BC) by ball milling for aqueous Cr (VI) removal and its mechanisms. *Journal of Hazardous Materials*, *413*, 125415.

Teklay, A. (2016). Physiological effect of chromium exposure: A review. *InterNational Journal of Food Sciences and Nutrients*, *7*, 1.

Wang, X., Xu, J., Liu, J., Liu, J., Xia, F., Wang, C., Dahlgren, R. A., & Liu, W. (2020). Mechanism of Cr (VI) removal by magnetic greigite/biochar composites. *Science of the Total Environment*, *700*, 134414.

Wang, B., Lan, J., Bo, C., Gong, B., & Ou, J. (2023). Adsorption of heavy metal onto biomass-derived activated carbon. *RSC Advances*, *13*, 4275.

Weber, W. J., Jr., & Morris, J. C. (1963). Kinetics of adsorption on carbon from solution. *Journal of the Sanitary Engineering Division*, *89*, 31–59.

Wen, Z., Zhang, Y., Cheng, G., Wang, Y., & Chen, R. (2019). Simultaneous removal of As (V)/Cr (VI) and acid orange 7 (AO7) by nanosized ordered magnetic mesoporous Fe-Ce bimetal oxides: Behavior and mechanism. *Chemosphere*, *218*, 1002–1013.

Yan, C. Z., Kim, M. G., Hwang, H. U., Nzioka, A. M., Sim, Y. J., & Kim, Y. J. (2020). Adsorption of heavy metals using activated carbon synthesized from the residues of medicinal herbs. *Theoretical Foundations of Chemical Engineering*, *54*, 973.

Yang, Y., Li, J., Yan, T., Zhu, R., Yan, L., & Pei, Z. (2020). Adsorption and photocatalytic reduction of aqueous Cr (VI) by Fe$_3$O$_4$-ZnAl-layered double hydroxide/TiO2 composites. *Journal of Colloid and Interface Science*, *562*, 493–501.

Yao, Y., Mi, N., He, C., Zhang, Y., Yin, L., Li, J., Wang, W., Yang, S., He, H., Li, S., & Ni, L. (2020). A novel colloid composited with polyacrylate and nano ferrous sulfide and its efficiency and mechanism of removal of Cr (VI) from Water. *Journal of Hazardous Materials*, *399*, 123082.

Younas, F., Mustafa, A., Farooqi, Z. U. R., Wang, X., Younas, S., Mohy-Ud-Din, W., Ashir Hameed, M., Mohsin Abrar, M., Maitlo, A. A., Noreen, S., & Hussain, M. M. (2021). Current and emerging adsorbent technologies for wastewater treatment: Trends, limitations, and environmental implications. *Water*, *13*, 215.

Yu, G., & Fu, F. (2020). Exploration of different adsorption performance and mechanisms of core-shell Fe$_3$O$_4$@Ce-Zr oxide composites for Cr (VI) and Sb (III). *Journal of Colloid and Interface Science*, *576*, 10–20.

Zhao, M., Cui, Z., Pan, D., Fan, F., Tang, J., Hu, Y., Xu, Y., Zhang, P., Li, P., Kong, X. Y., & Wu, W. (2021). An efficient uranium adsorption magnetic platform based on amidoxime-functionalized flower-like Fe$_3$O$_4$@TiO$_2$ core–shell microspheres. *ACS Applied Materials & Interfaces*, *13*, 17931–17939.

Zou, H., Zhao, J., He, F., Zhong, Z., Huang, J., Zheng, Y., Zhang, Y., Yang, Y., Yu, F., Bashir, M. A., & Gao, B. (2021). Ball milling biochar iron oxide composites for the removal of chromium (Cr (VI)) from water: Performance and mechanisms. *Journal of Hazardous Materials*, *413*, 125252.